Evaluation of the overset grid method for control studies of wave energy converters in OpenFOAM numerical wave tanks

Journal of Ocean Engineering and Marine Energy (2020) 6:55–70
https://doi.org/10.1007/s40722-019-00156-5

RESEARCH ARTICLE

# Evaluation of the overset grid method for control studies of wave energy converters in OpenFOAM numerical wave tanks

Christian Windt[1] · Josh Davidson[2] · Dominic D. J. Chandar[3] · Nicolás Faedo[1] · John V. Ringwood[1]

Received: 14 September 2019 / Accepted: 1 December 2019 / Published online: 16 December 2019


**Abstract**
Computational fluid dynamics (CFD)-based numerical wave tanks are valuable tools for the development and evaluation of energy maximising control systems for wave energy converters (WECs). However, the exaggerated body motion amplitude, which can be induced by the energy maximising control system, challenges the commonly applied mesh morphing method in CFD, due to the resulting mesh distortion and subsequent numerical instability. A more advanced mesh motion method is the overset grid method, which can inherently handle large-amplitude body motions and has recently become freely available in the open-source CFD software OpenFOAM. The overset grid method can, therefore, potentially eliminate the mesh distortion problem, hindering the simulation of WECs under controlled conditions. To evaluate the capability of the overset grid method for control studies of WECs in an OpenFOAM numerical wave tank, this paper presents a detailed comparison of the overset grid and mesh morphing methods, considering five test cases of increasing complexity. The test cases range from a static equilibrium test to the modelling of a controlled WEC, and good agreement is demonstrated between the two mesh motion methods, except for the case of the controlled WEC, when the device motion becomes large, and the mesh morphing simulation crashes. The runtimes for overset grid simulations are observed to be approximately double the time required for the mesh morphing simulations.

**Keywords** Mesh motion · Overset grids · Numerical wave tank · Energy maximising control · OpenFOAM

## 1 Introduction

Throughout the last decades, an increased effort, in the research and development (R&D) of novel technologies to harness various renewable energy resources, can be observed. Among the developing technologies, offshore renewable energies, and specifically ocean wave energy, show significant potential to contribute to the global energy supply (Falcao 2010).

In wave energy research, engineers rely on small-scale physical wave tank tests, small- and/or full-scale numerical wave tank tests, as well as large-scale open ocean trials. While open ocean trials are associated with significant costs for the construction, deployment, operation, and maintenance of the prototype, experiments in physical wave tanks and numerical wave tanks are cheaper to conduct and, furthermore, allow testing in a more controlled environment. Thus, at low- to mid-technology readiness levels (TRLs) (Mankins 1995), physical wave tanks and numerical wave tanks are the most important tools for the WEC development, complementing each other. Generally, by testing in a real physical environment, physical wave tanks allow all the relevant details of the wave–structure interaction (WSI) to be captured. However, although still cheaper compared to open ocean trials, physical wave tank experiments are associated with higher costs compared to numerical wave tank experiments, when many design iterations are required (Kim et al. 2016). The main cost drivers are instrumentation, construction of the prototype, test facilities, and staff. Additionally, the accuracy of physical wave tank experiments potentially suffers from peculiarities of the test facility, such as reflections from the tank walls,

✉ Christian Windt
christian.windt.2017@mumail.ie

1 Centre for Ocean Energy Research, Maynooth University, Maynooth, Co. Kildare, Ireland

2 Department of Fluid Mechanics, Faculty of Mechanical Engineering, Budapest University of Technology and Economics, Budapest, Hungary

3 School of Mechanical and Aerospace Engineering, Queen's University Belfast, BT7 1NN Belfast, Northern Ireland, UK

unwanted friction in mechanical restraints/constraints, measurement errors/noise, and scaling effects.

Overcoming the drawbacks of high costs, measurement noise, mechanical friction (Windt et al. 2019c) and, to a great extent, scaling effects (Windt et al. 2019f), numerical wave tanks provide powerful tools for the analysis of WECs. A range of numerical models, with varying computational cost and fidelity, are available for WSI problems (Penalba et al. 2017a). Lower-fidelity models, based on linear hydrodynamic modelling techniques, such as boundary element method-based numerical wave tanks, are computationally efficient; however, the accuracy of low fidelity models decreases drastically when the amplitude of the waves and the WEC motion increases, and, thereby, violates the validity of the underlying linearising assumptions (Giorgi and Ringwood 2017). To broaden the range of validity, linear models can be extended to capture non-linear effects, such as viscous drag or non-linear Froude–Krylov forces. Next, mid-fidelity models, such as fully non-linear potential flow solvers, still assume irrotational and inviscid fluid but are able to capture non-linear free-surface deformations. Finally, higher-fidelity models, such as CFD-based numerical wave tanks, deliver accurate results over a wide range of test conditions by including the relevant non-linear hydrodynamic effects, at the expense of increased computational cost (Folley 2016).

The relative strengths and weaknesses of the various numerical models can be leveraged at different stages of the device R&D. During early stage development, lower-fidelity models are suitable for parametric studies, where a vast number of simulations are required to cover a broad parameter space. At higher TRLs, the system under investigation becomes more refined and a higher level of accuracy is required to evaluate the performance of the system. The use of a high-fidelity model has been shown to be particularly vital for the accurate assessment of energy maximising control systems, which drive the WEC into resonance with the incoming wave field, resulting in large-amplitude motions (see Fig. 1), beyond the limits within which lower fidelity models are reliable (Davidson et al. 2018; Giorgi et al. 2016; Ringwood et al. 2014).

Although the fidelity of a CFD-based numerical wave tank is well suited for the evaluation of energy maximising control system (Davidson et al. 2018), large-amplitude body motion can introduce numerical instabilities due to the required, explicit, accommodation of the device motion in the finite volume domain. A number of different dynamic mesh motion methods are available, whose usage and suitability for WEC experiments are reviewed by Windt et al. (2018b). Among these methods, the overset grid method shows particular potential for handling large-amplitude, multi-degree of freedom, WEC motion (Windt et al. 2018a, 2019a). The overset grid method, implemented in the OpenFOAM CFD toolbox *opera*, developed at the Institute Of High Performance Computing, Singapore (Chandar 2019), is used here to assess its feasibility for WEC control studies.

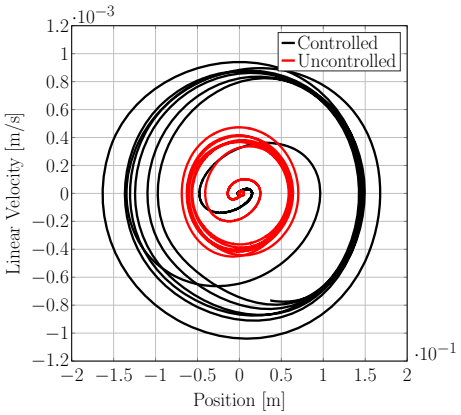


**Fig. 1** Operational space of an uncontrolled and controlled WEC device (Windt et al. 2019b), with zero initial conditions and under regular wave excitation: The linear velocity of the WEC in the heave degree of freedom is plotted over the WEC position in the heave degree of freedom

## 1.1 Related studies

To date, only a relatively small number of studies have employed the overset grid method for CFD-based numerical wave tank WEC experiments (Stansby et al. 2015; Coiro et al. 2016; Elhanafi et al. 2017a, b; Bharath et al. 2018; Windt et al. 2018a, 2019a; Chen et al. 2019a, b; Coe et al. 2019; van Rij et al. 2019). The limited use of the overset grid method in the wave energy field can be attributed to:

1. The significantly higher computational cost (Jung and Kwon 2009)
2. The introduction of numerical errors in the volume of fluid environment, such as violation of mass conservation (Chandar 2019; Ferziger and Peric 2001)
3. The limited availability of the overset grid method in commonly used CFD software.

Until recently, the overset grid method was only available in commercial CFD software packages. All of the initial WEC-related studies, which employed the overset grid method, were implemented in the commercial CFD solver (STAR-CCM+ 2019).

The first study was conducted by Stansby et al. (2015), investigating drag effects on the performance of the *M4* WEC for different floater shapes. Forced oscillation tests were performed in a CFD-based numerical wave tank to determine the drag coefficient term, $C_d$, in the Morrison equation (Morison et al. 1950). The authors point out that a decrease in $C_d$ can be achieved by changing the shape of the floater, which,

in turn, results in better performance. Some discrepancy is found between the experimental and numerical results for $C_d$; however, no quantitative validation of the CFD-based numerical wave tank is presented.

Similarly, Coiro et al. (2016) perform CFD-based numerical wave tank experiments, employing the overset grid method, to evaluate the influence of viscous effects on the performance of a point-pivoted WEC. The authors indicate *worrying* mismatch, compared to physical wave tank data, for some system characteristics, such as the natural frequency of the WEC. Unfortunately, no further investigation of the cause of the mismatch is provided.

Elhanafi et al. (2017a, b) investigate the performance and survivability of a floating-moored oscillating water column device. Numerical results for the device motion, generated power, and mooring line tension, for a 1:50 scale model, are compared to physical wave tank data. The authors find good agreement between the numerical and experimental results, with an overall maximum normalised root mean square deviation of 14.6%.

Bharath et al. (2018) perform numerical simulation of diffraction and radiation experiments, for a spherical WEC, operating in heave and surge degrees of freedom (DoF). Numerical results from CFD simulations are compared to lower-fidelity numerical models, as well as physical wave tank data. The authors find good agreement between the CFD-based numerical wave tank and physical wave tank results, and identify free-surface effects as the main cause of differences between CFD-based and lower-fidelity numerical models.

Coe et al. (2019) perform a design-load analysis of a two-body WEC, the *Triton*, employing the overset grid method to account for the relative motion of the two bodies. Monochromatic and focused waves are modelled to analyse design-load conditions, showing that focused waves result in larger loads, compared to equivalent monochromatic waves.

Also performing a design-load analysis, van Rij et al. (2019) consider the so-called RM3 WEC. The authors evaluate structural loads on the device at three different levels of computational fidelity: low-, mid-, and high fidelity. For the high-fidelity simulations, the CFD solver is coupled with a finite element solver, for which good agreement between experimental and numerical results is found. The authors conclude that the numerical model can deliver reliable design-load data.

More recently, the availability of the overset grid method in CFD software has been improved via the code release of the overset grid method for the open-source CFD toolbox OpenFOAM v1706 and later, making it freely available to a wider user community. However, overset grids in OpenFOAM have, to date, only been applied for WEC experiments by Windt et al. (2018a, 2019a) and Chen et al. (2019a, b).

Chen et al. (2019a) show a number of different hydrodynamic free-surface problems, modelled using the overset grid method, implemented in OpenFOAM v1706. A free decay test of a locked self-reacting floating point absorber is modelled. A qualitative and quantitative analysis is presented for the radiated waves and the heave decay, respectively. For the heave decay, sufficient agreement with the available experimental data is found.

Chen et al. (2019b) furthermore present a contribution to the Blind Test Series 3 of the Collaborative Computational Project in Wave Structure Interaction, using the overset grid method, implemented in OpenFOAM v1706. Since experimental data were inaccessible at the time of publication, no validation is presented.

In a previous study (Windt et al. 2018a) by the authors of the present paper, the performance of the overset implementation in OpenFOAM version v1706 is assessed, comparing free decay experiments of a scaled model of the *Wavestar* WEC against physical wave tank experiments. Major drawbacks, in terms of accuracy of the solution, computational overhead, and parallelisation of the solution process are revealed. Subsequent to the publication by Windt et al. (2018a), improvements to the overset grid method have been implemented and released in OpenFOAM v1712 and v1812; namely, improved parallel computation through better performance of the momentum predictor and revised decomposition tolerances in v1712 (ESI 2017), as well as revised pressure–velocity coupling in v1812 (ESI 2018). The updated overset grid method in v1812 is assessed by Windt et al. (2019a), finding a significant improvement compared to the initial v1706 implementation assessed (Windt et al. 2018a) and, thus, showing potential for the application of WEC experiments, specifically for control studies. In Windt et al. (2019a), the overset implementation in v1812 is also compared to the in-house overset toolbox, *opera* (Chandar 2019). While the two overset implementations are found to display good agreement in terms of WEC motion, *opera* shows considerably better computational efficiency.

### 1.2 Objectives

The objectives of the current paper stem from the findings by Windt et al. (2019a), which identify the following as pertinent future work:

(a) Further evaluation of the *opera* overset grid implementation in OpenFOAM.
(b) The application of the overset grid method to WEC control studies.

The preliminary study by Windt et al. (2019a) only presents a single test case when comparing the results between the mesh morphing and the overset grid method,

considering the motion of an uncontrolled WEC subjected to an irregular wave series. The current paper provides more in-depth comparative studies, based on an array of test cases with increasing complexity: (1) a static equilibrium test, (2) a heave free decay test, (3) a wave excitation force test, (4) a wave-induced motion test of an uncontrolled device in regular waves, and (5) a wave-induced motion test of a controlled device in irregular waves. This paper presents the first study modelling a moored point-absorber-type WEC, under controlled conditions, in the OpenFOAM environment with overset grids. The employed controller is designed based on a recently proposed moment-based control strategy proposed by Faedo et al. (2018).

### 1.3 Outline of the paper

The remainder of the paper is organised as follows. Section 2 briefly introduces the two dynamic mesh motion methods, mesh morphing and overset grids, used throughout this study. Subsequently, Sect. 3 details the case studies, while the CFD-based numerical wave tank setup is described in Sect. 4. Results of the comparative study between mesh morphing and overset grids for the five assessment test cases are presented and discussed in Sect. 5. Finally, conclusions are drawn in Sect. 6.

## 2 Dynamic mesh motion methods

Several dynamic mesh motion methods are available to accommodate moving bodies in CFD-based numerical wave tank simulations. For WEC simulations, the review by Windt et al. (2018b) identifies mesh morphing as the most commonly used dynamic mesh motion method, due to its relative simplicity and general applicability. More advanced methods are re-meshing, sliding mesh interfaces, or overset grids. The latter is attracting increased attention, due to its capability of easily handling multi-body, multi-DoF motion with arbitrarily large amplitudes, which opens the way for WEC experiments that were previously infeasible in CFD-based numerical wave tanks, as discussed by Davidson et al. (2019).

This section will introduce the two dynamic mesh motion methods employed in this paper, i.e., mesh morphing (Sect. 2.1) and overset grids (Sect. 2.2). For further insight, the interested reader is referred to the presented references.

### 2.1 Mesh Morphing

In a finite volume method algorithm, if grid connectivity should be retained (meaning no topological changes), mesh morphing is the classical method to accommodate body motion in the computational domain. In the *sixDoFRigidBodyMotion* solver in OpenFOAM, the spherical linear interpolation (SLERP) algorithm is implemented to calculate the mesh displacement based on the distance of a cell to the moving body, which gives control over the grid quality during mesh deformation (OpenFOAM Foundation 2014). As depicted in Fig. 2, the displacement of the body leads to a deformation of single control volumes, while the total volume of all control volumes in the domain remains constant throughout the simulation. The user specifies an *inner* and *outer* distance, between which mesh deformation is allowed and prohibited elsewhere (see Fig. 2).

For large translational WEC displacements, moderate rotational WEC displacements, or multiple bodies moving in close proximity, the deformation of the original, good-quality, mesh can lead to poor grid quality, such as large aspect ratios and/or highly skewed, non-orthogonal cells, resulting in numerical instability and, ultimately, causing the simulation to crash.

The reduction in mesh quality depends on the layout of the numerical domain, the choice of the inner and outer distances, and the amplitude of the body motion. If the amplitude of the body motion is (roughly) known a priori, the simulation can be set up such that the likelihood of numerical instability from mesh distortion is reduced. However, if the dynamics are not known a priori, time-consuming preliminary studies must be performed.

This weakness of the mesh morphing method, in handling large displacements, limits the range of allowable motion in WEC experiments. This is especially true for rotational DoFs, which commonly forces studies to constrain rotational modes of motion and consider WECs moving only in heave, for example. Certain sea states, or control settings, which result in large resonant WEC motions, can not be simulated, due to the numerical instability caused by the degradation in mesh quality. However, it is these sea states and conditions where the CFD-based numerical wave tank is required most, since the large resonant motions lead to non-linearities, not captured by lower-fidelity simulation models

### 2.2 Overset grids

In the overset grid method, (at least) two grids (background and body-fitted) are defined, which may arbitrarily overlay

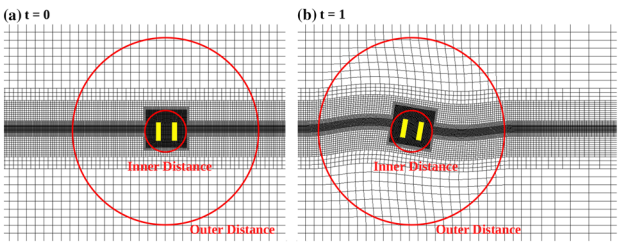


**Fig. 2** Idealised illustration of the mesh morphing method. In the area between inner and outer distance mesh deformation is allowed

each other (see Fig. 3). The different grids are internally static, thereby retaining their original structure and quality, but are allowed to move relative to each other. To pass information between the different grids, interpolation must be performed. The overset grid method can be split into the four sequential steps:

1. Identification of hole cells
2. Identification of fringe cells
3. Identification of donor cells
4. Interpolation between fringe and donor cells

Hole cells embrace cells in the background grid, lying inside the moving body. These cells are marked and blanked out during the solution process. This step is the main cause for the extensive computational cost of the overset grid method (Thompson 1999). In the second step, cells adjacent to hole cells are identified as fringe cells. Likewise, cells at the outer boundary of the body-fitted grid are also identified as fringe cells. These cells are used as boundary cells in the solution procedure. Boundary values for fringe cells are determined through solution interpolation. In the third step, the interpolation partners on both grids, the donor cells, are identified. Lastly, interpolation between fringe and donor cells is performed. For dynamic simulation, all steps have to be performed at every time step. The quality of the numerical results is directly impacted by these four steps, and therefore depends on the employed interpolation scheme and the problem discretisation in the background and body-fitted grid.

The major advantage of the overset method is that large-amplitude motion in multiple DoFs is possible, with the mesh structure and quality remaining constant throughout the simulation. This has been used, for example, to simulate ship motion, with a moving rudder and a spinning propeller, using separate overset grids for the hull, rudder and propeller (Shen et al. 2015).

The disadvantage of the overset grid method is the increase in computational time, due to steps (1)–(4) described above. Additionally, interpolation of field variables (e.g., $\alpha$, $p$, etc.) between grids can lead to conservation and convergence issues, and represents the biggest challenge of the overset grid method (Ferziger and Peric 2001). For multi-phase problems, the conservation issues can result in artificial water convection, indicated by a change of the water level. For a detailed analysis of interpolation strategies and their implications on the solution accuracy, the interested reader is referred to Chandar (2019).

## 3 Case studies

This section presents the case studies, used to assess the performance of the *opera* overset grid method, and to model a WEC under controlled conditions. Section 3.1 describes the considered WEC, Sect. 3.2 presents the input waves, used for the different WSI simulations, and Sect. 3.3 details the proposed tests for the assessment of the overset grid method.

### 3.1 WEC device

The WEC device is based on the system considered for the Blind Test Series 3 of the Collaborative Computational Project in Wave Structure Interaction (Ransley et al. 2019), which comprises an axisymmetric, cylindrical buoy, featuring a sharp-cornered bottom and a moon-pool (see Fig. 4). All relevant geometrical dimensions of the WEC are shown in Fig. 4 and the inertial properties listed in Table 1. The buoy is moored to the tank floor, using a linear spring, with a stiffness of 67 N m$^{-1}$. A mooring pretension, based on the spring stiffness, the draft, and buoyancy properties of the system, of 31.55N is measured. It should be noted that the presented WEC device serves as a realistic example for the present study; however, no comparison to experimental data is presented herein.

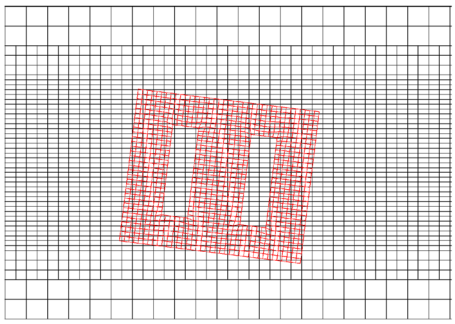

**Fig. 3** Illustration of the overset grid method. Background mesh in black; overset mesh in red

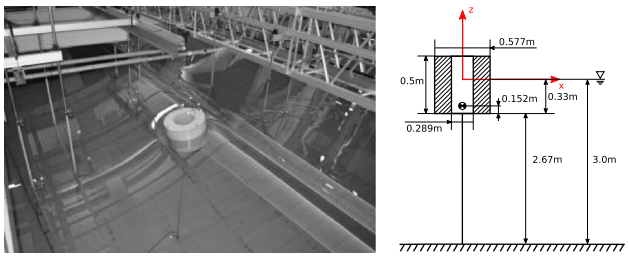


**Fig. 4** Photograph and schematic of the considered WEC, including the main dimensions

**Table 1** Inertial properties of the considered WEC

| Property | Unit | Value |
|---|---|---|
| Mass | (kg) | 61.459 |
| Ixx | (kg m$^2$) | 3.56 |
| Iyy | (kg m$^2$) | 3.56 |
| Izz | (kg m$^2$) | 3.298 |

### 3.2 Input waves

In the case studies, both regular and irregular, JONSWAP, sea states are considered, with a (significant) wave height of $H_s = 0.12$m and (peak) period of $T_p = 1.94$s. The wave characteristics are chosen based on the scatter diagram of the AMETS test site in Bellmullet, Co. Mayo, off the West Coast of Ireland. Compared to other test site (e.g. BIMEP, SEMREV), AMETS is characterised by relatively large wave heights (Penalba et al. 2017b; Atan et al. 2016). A full-scale irregular sea state[1] with a significant wave height, $H_s$, of 3.5 m, and a peak period, $T_p$, of 10.6 s shows the highest occurrence (Sharkey et al. 2011).

For the Blind Test Series 3, the WEC device was tested in a physical wave tank with 3 m water depth. Thus, Froude scaling with a scaling factor of 1/30th is applied, to retain deep water conditions of the AMETS site. This results in the scaled $H_s$ of 0.12 m, and a $T_p$ of 1.94 s.

Time traces of the recorded free-surface elevation, measured in the CFD-based numerical wave tank at the intended WEC location, during a preliminary wave-only simulation, as well as the according spectral density distribution, are shown in Fig. 5a, b, respectively, for the regular sea state, and for the irregular sea state in Fig. 6a, b, respectively.

### 3.3 Assessment of the overset grid method

For the assessment of the overset grid method, five different test cases, of increasing complexity, are considered, detailed in Sects. 3.3.1–3.3.5.

#### 3.3.1 Static equilibrium test

To test the numerical stability of the solver, a simple test case of a floating WEC initialised in its equilibrium position, without external excitation (e.g., input waves), is simulated for a duration of 10 s. The simulated body position and the resulting hydrodynamic forces are compared between the mesh morphing and overset grid methods.

#### 3.3.2 Free decay test

In a next test case, the WEC is initialised away from its equilibrium position, in the form of an initial heave displacement of 0.05 m. No input waves are considered for the test case, so that an oscillatory, decaying, motion around the device's equilibrium position is expected. Again, the simulated body motions and the resulting hydrodynamic forces are compared between the mesh morphing and overset grid methods.

#### 3.3.3 Wave excitation forces test

To introduce WSI in the assessment of the overset grid method, wave excitation force experiments are considered. Regular waves are created by a numerical wave maker, propagate through the domain, and interact with the WEC device, which is held fixed at its equilibrium position. For the assessment of the overset grid method, the excitation forces on the body are post-processed and compared with results from the mesh morphing method. Holding the body fixed in this test eliminates any dynamic mesh motion from the experiment, therefore, any difference between the two sets of results indicates interpolation errors in the overset grid method between the background and overset mesh.

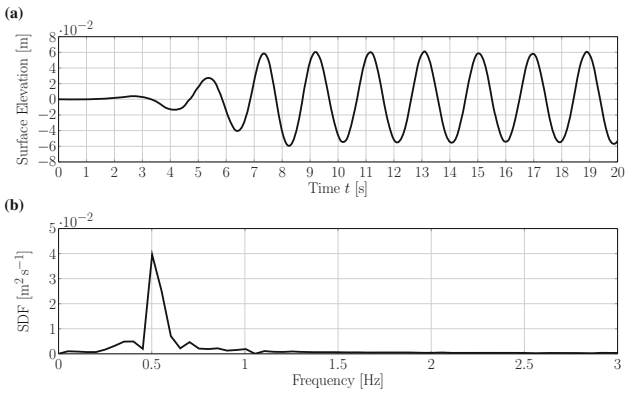


**Fig. 5** Surface elevation time trace and the corresponding spectral density distribution of the regular, 2nd order Stokes wave

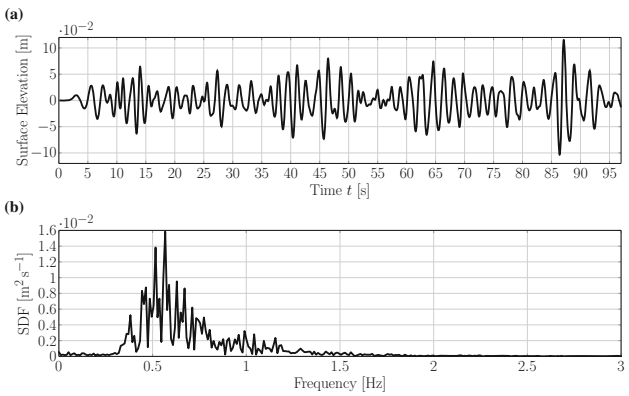


**Fig. 6** Surface elevation time trace and the corresponding spectral density distribution of the irregular sea state

[1] Unlike a regular sea state, an irregular sea state refers to a free-surface elevation time trace which is composed of a finite sum of harmonics of a sufficiently small fundamental frequency $\omega_0$ (Mérigaud and Ringwood 2017), serving as a numerical approximation to real panchromatic (continuous spectrum) seas.

#### 3.3.4 Wave-induced motion—uncontrolled WEC

As a first test of wave-induced WEC motion, regular waves are created by a numerical wave maker, similar to the wave excitation force test, propagate through the domain, and interact with the WEC device. However, in this test case, the uncontrolled WEC device is now allowed to move in three DoF, i.e. heave, surge, and pitch. The simulated body motions and the hydrodynamic forces are compared between the mesh morphing and overset grid methods.

#### 3.3.5 Wave-induced motion—controlled WEC

Finally, the performance of the overset grid method is assessed for a WEC in operational conditions. A power take-off (PTO) system is implemented in the CFD-based numerical wave tank as a linear spring-damper system. The implementation of the PTO allows the WEC to be controlled using a reactive output-feedback controller.

The energy maximising optimal controller, considered in this study, is synthesised in an output-feedback form,[2] using both displacement and velocity of the device as measurable variables. To be precise, an optimal control law $u : \mathbb{R}^+ \longrightarrow \mathbb{R}$ written in a parametric form

$$u(t) = -k_u z(t) - b_u \dot{z}(t), \tag{1}$$

with $\mathscr{H} = \{k_u, b_u\} \subset \mathbb{R}$, is applied to the WEC, realised by means of the PTO system, where $z(t)$ and $\dot{z}(t)$ represent the heave displacement and velocity of the device, respectively. This set of energy maximising optimal parameters $\mathscr{H}$ is computed using the *moment-based* optimal control framework developed by Faedo et al. (2018). Briefly summarised, this model-based strategy uses an efficient parameterisation of the system variables in terms of the so-called *moments* of the analysed system, which are intrinsically related to the steady-state response mapping of the WEC for a given wave input (Faedo et al. 2018; Windt et al. 2019h). The resulting optimisation procedure guarantees maximum power extraction from a given sea state for the parametric form (1), while securing the internal stability of the closed-loop (in the Lyapunov sense (Goldhirsch et al. 1987)), as a direct consequence of this moment-based parameterisation and the system-theoretic approach considered.

To assess the influence of the controller on the device dynamics, and, ultimately, on the dynamic mesh motion method, simulations of a uncontrolled (i.e., no PTO) and controlled WEC are performed and compared using mesh morphing and overset grids. For these test cases, the simulated body motions are monitored and compared.

[2] The reader is referred to (Goodwin et al. 2001, Chapter 2) for further detail on the fundamentals behind feedback control techniques.

## 4 Numerical wave tank setup

In this section, the CFD-based numerical wave tank setup is detailed. The governing equations are presented (Sect. 4.1), as well as the treatment of numerical wave generation and absorption (Sect. 4.2), and the specifics for the two different dynamic mesh motion methods utilised: mesh morphing (Sect. 4.4) and the overset grid method *opera* (Sect. 4.5).

### 4.1 Governing equations

The hydrodynamics in the CFD-based numerical wave tank are modelled by solving the incompressible Reynold Averaged Navier–Stokes (RANS) equations, describing the conservation of mass (Eq. (2)) and momentum (Eq. (3)).

$$\nabla \cdot \mathbf{U}(t) = 0, \tag{2}$$

$$\frac{\partial \rho \mathbf{U}(t)}{\partial t} + \nabla \cdot \rho \mathbf{U}(t)\mathbf{U}(t) = -\nabla p(t) + \nabla \cdot \mathbf{T}(t) + \rho \mathbf{f}_b(t) + u(t). \tag{3}$$

In Eqs. (2) and (3), $t$ denotes time, $\mathbf{U}(t)$ is the fluid velocity, $p(t)$ the fluid pressure, $\rho$ the fluid density, $\mathbf{T}(t)$ the stress tensor, and $\mathbf{f}_b(t)$, the external forces, such as gravity. $u(t)$ is the control input. The water wave advection is captured via the volume of fluid method, proposed by Hirt and Nichols (1981), following:

$$\frac{\partial\, \alpha(t)}{\partial\, t} + \nabla \cdot (\mathbf{U}(t)\alpha(t)) + \nabla \cdot [\mathbf{U}_\mathrm{r}(t)\alpha(t)(1-\alpha(t))] = 0, \tag{4}$$

$$\Phi(t) = \alpha(t)\Phi_\mathrm{water}(t) + (1-\alpha(t))\Phi_\mathrm{air}(t), \tag{5}$$

where $\alpha(t)$ denotes the volume fraction of water, $\mathbf{U}_\mathrm{r}(t)$ is the relative velocity between liquid and gaseous phase (Berberović et al. 2009), and $\Phi(t)$ is a specific fluid quantity, such as density.

### 4.2 Numerical wave generation and absorption

The IHFOAM (Higuera et al. 2013) toolbox is employed for wave generation and absorption. IHFOAM is readily implemented in OpenFOAM v1812, and can be classified as a static boundary method (Windt et al. 2019g). Waves are generated at the up-wave boundary of the CFD-based numerical wave tank, by prescribing the target water level, through the water volume fraction, and the fluid velocity. For an irregular sea state, the wave amplitudes and phases for each frequency component of the wave act as inputs to the wave maker. For wave absorption, a correction velocity, based on shallow water theory, is imposed at the down-wave domain boundary, to cancel out the incoming wave.

To measure the free-surface elevation, the iso-surface of the volume fraction $\alpha(t) = 0.5$ is recorded throughout the course of the simulation, and can be extracted at specific locations in a post-processing step.

### 4.3 Turbulence modelling

To account for turbulence, a RANS turbulence model, specifically the standard $k$-$\omega$ SST turbulence model (Menter 1992), with industry standard, high Reynolds number, wall functions is employed for the wave-induced motion test of the controlled WEC. The choice of the turbulence model is based on the literature review presented by Windt et al. (2018b), in which the $k$-$\omega$ SST turbulence model is identified as one of the most commonly used turbulence models in the field of ocean wave energy. For brevity, the governing equations of the $k$-$\omega$ SST turbulence model are not presented here. The interested reader is referred to Menter (1992). It should be noted here that the application of turbulence modelling for WECs is still an active field of research. As pointed out by Schmitt and Elsässer (2017), in oscillating flows, the value of $y^+$ changes through a wave cycle[3] and, thus, no single grid size can be found to comply with the requirements posed on $y^+$. The time-variance of $y^+$, $0 < y^+ \leq 500$ for the present case, and, thus, the time-varying validity of wall functions, must be considered when analysing simulations of oscillating flows which include turbulence modelling.

Turbulence modelling is only considered for the simulations of the last assessment test case, wave-induced motion of the controlled WEC. Under controlled conditions, it is assumed that turbulent effects are of importance. For the cases under controlled conditions, maximum Keulegan–Carpenter (KC) number[4] of approx. 10 can be found. For all other test cases, laminar flow conditions are assumed, to reduce the computational overhead for the comparative study between the mesh morphing and overset grid methods.

### 4.4 Mesh morphing

In this section, the setup of the CFD-based numerical wave tank employing mesh morphing will be described, which is adapted from (Windt et al. 2019a, e) and validated in (Ransley et al. 2019; Windt et al. 2019d). The CFD-based numerical wave tank spans a length of $3.5\lambda_\mathrm{p}$ (in the $x$-direction, see Fig. 7) and $1.3\lambda_\mathrm{p}$ in the $y$-direction, perpendicular to the wave propagation direction. In the $z$-direction, the CFD-based numerical wave tank spans $2d$, where $d$ is the water depth. The still water line is located at $z = 0$. The structure is located $1.2\lambda_\mathrm{p}$ down-wave from the wave generation boundary, and $2.3\lambda_\mathrm{p}$ up-wave from the absorption boundary, corresponding to $(x, y, z) = (0, 0, 0)$.

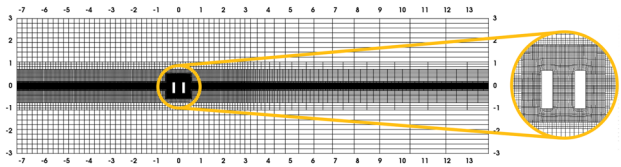

**Fig. 7** Two-dimensional (2D) slice ($xz$-plane) of the spatial problem discretisation. The WEC device is located at $(x, y, z) = (0, 0, 0)$

The symmetry of the problem is exploited, and a symmetry boundary condition is applied in the $xz$-plane, at $y = 0$. This imposes constraints on the motion of the device, only allowing translational motion in surge and heave, as well as rotational motion in pitch. Since only unidirectional, long crested waves are considered in this study, the sway, roll and yaw DoFs are negligible. The inner distance for the mesh morphing method is set to 0.05m, while the outer distance is set to 1.5 m, i.e., approx. 3 device diameters. Note that the outer distance is chosen based on the optimal distance between controlled WECs as indicated by Balitsky et al. (2014) and Garcia-Rosa et al. (2015).

#### 4.4.1 Convergence study

To determine the converged spatial and temporal discretisation size, i.e., time step and cell size, convergence studies are performed on the basis of the regular wave, described in Sect. 3.2. For the spatial discretisation, the smallest cell size in the $z$-direction, around the free-surface interface, has been parametrised by the wave height. Three different cell sizes, i.e., 5 cells per wave height (CPH), 10CPH, and 20CPH are tested. In the interface region, the mesh features a horizontal to vertical aspect ratio of 2. Towards the down-wave boundary of the CFD-based numerical wave tank, cell stretching is applied to enhance the wave absorption and reduce the overall cell count. In the $y$-direction, cells feature an aspect ratio of 1, over a length of $2R$, where $R$ is the device radius. Further away from the structure, i.e., $y \geq 2R$, cell stretching is applied (Table 2).

For the convergence studies, the measured wave height has been extracted from the simulations through phase averaging (Windt et al. 2019g). Table 3 shows the result of the spatial convergence study. With a fixed time step of $\Delta t = 0.002$ s, oscillatory convergence can be found for a cell size of $\Delta z =$ 10CPH. The relative grid uncertainty $\bar{U}$ is 1.32%.

For the temporal convergence study, the cell size in the interface region $\Delta z$ is fixed to 10CPH. Three different (fixed) time step sizes, i.e., $\Delta t = 0.004$ s, 0.002 s, 0.001 s, are con-

[3] $y^+$ is defined as $\frac{u_* \cdot y}{\nu}$, where $u_*$ describes the friction velocity, $y$ is the distance to the nearest wall, and $\nu$ denotes the kinematic viscosity.

[4] KC is defined as $\frac{u_m \cdot T}{L}$, where $u_m$ is the amplitude of the (oscillating) flow velocity, $T$ the oscillation period, and $L$ the characteristic length scale. Here, the oscillation periods is considered to be $T_p$ and the length scale is the wall thickness of the structure.

**Table 2** Results of the temporal convergence study

| $\Delta z$ | Absolute wave height | | | Convergence type | $\bar{U}$ |
|---|---|---|---|---|---|
| | $\Delta t$ 0.004s | $\Delta t$ 0.002s | $\Delta t$ 0.001s | | |
| 10CPH | 0.108 m | 0.113 m | 0.115 m | Monotone | 1.74% |

**Table 3** Results of the spatial convergence study

| $\Delta t$ | Absolute wave height | | | Convergence type | $\bar{U}$ |
|---|---|---|---|---|---|
| | $\Delta z$ 5CPH | $\Delta z$ 10CPH | $\Delta z$ 20CPH | | |
| 0.002 s | 0.111 m | 0.113 m | 0.112 m | Oscillatory | 1.32% |

sidered. Again, the phase averaged wave height is used as the input for the convergence study. Table 2 shows the results of the temporal convergence study. With a cell size in the interface region of $\Delta z$ =10CPH, monotonic convergence can be found for a time step size of $\Delta t = 0.002$ s. The relative grid uncertainty $\bar{U}$ is 1.74%.

To ensure converged solutions for the body motion, a spatial convergence study is also performed for the grid size around the body. Three different grid sizes, equivalent to 5, 10, and 20 CPH are considered and the root mean square values of the heave motion are used as input for the convergence study. The results are listed in Table 4. Monotonic convergence can be found with a relative grid uncertainty $\bar{U} = 0.26\%$. Generally, it is desirable to use uniform meshes in the interface region to prevent spurious velocities in the interface region, induced by cell nodes hitting cell faces. Overall, the results of the presented convergence studies, for the spatial and temporal discretisation sizes, are consistent with the reviewed literature in (Windt et al. 2018b).
A screenshot of the spatial discretisation of the CFD-based numerical wave tank is shown in Fig. 7. The field variable $\alpha$, at time $t = 0$, is depicted in Fig. 8.

## 4.5 Overset grid

The setup of the CFD-based numerical wave tank, for the overset grid simulations, follows the setup outlined by Windt et al. (2019a). The domain comprises a background (black colour code in Fig. 9) and an overset mesh (red colour code in Fig. 9). The dimensions, as well as the spatial discretisation of the background mesh, are the same as for the mesh morphing CFD-based numerical wave tank, and the symmetry boundary condition is also applied in the $xz$-plane, at $y = 0$. The overset mesh region, spans $1.6R \times 1.6R \times 0.9R$ in the $x$-, $z$-, and $y$-directions. The discretisation in the overset mesh has been chosen to reflect a similar discretisation around the WEC device, as in the mesh morphing CFD-based numerical wave tank. The device is located in the centre of the overset mesh.

### 4.5.1 Opera

For this study, the in-house overset grid toolbox *opera* is employed, based on the results from the study by Windt

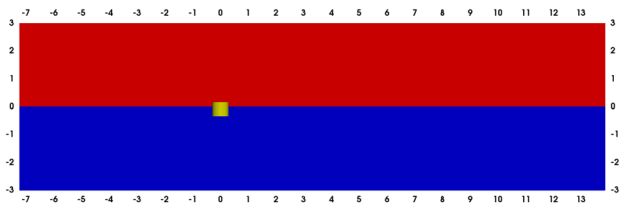

**Fig. 8** 2D slice ($xz$-plane) of the CFD-based numerical wave tank. The water (blue) and air (red) phase are depicted, together with the WEC device (yellow)

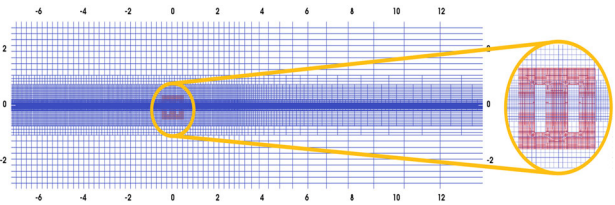

**Fig. 9** 2D slice ($xz$-plane) of the CFD-based numerical wave tank for the overset grid method, where the background mesh is blue, the overset region is red

**Table 4** Results of the spatial convergence study

| $\Delta t$ | Absolute wave height | | | Convergence type | $\bar{U}$ |
|---|---|---|---|---|---|
| | $\Delta z$ 5CPH | $\Delta z$ 10CPH | $\Delta z$ 20CPH | | |
| 0.002 s | $3.33 \times 10^{-2}$ m | $3.36 \times 10^{-2}$ m | $3.37 \times 10^{-2}$ m | Monotone | 0.26% |

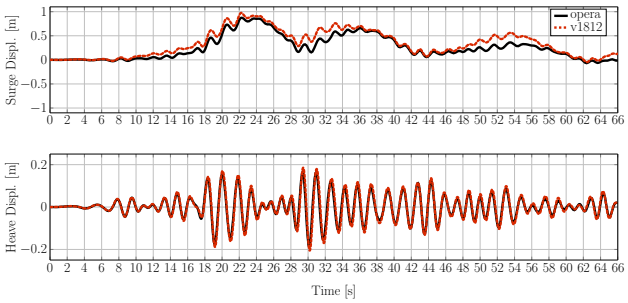


**Fig. 10** Heave and surge displacements of a WEC, exposed to irregular waves, from simulations performed with *opera* and the native overset grid implementation in OpenFOAM v1812

et al. (2019a). Compared to the native overset grid method in OpenFOAM v1812, three main differences can be identified in *opera*:

1. The donor search algorithm uses a dual-level parallelism approach, for increased computational efficiency.
2. The interpolation layers on the near body mesh are two-layered, avoiding the need for the interpolation of gradients.
3. The inverse distance interpolation algorithm has been improved.

For a more detailed description of the *opera* algorithm, and some performance assessment studies, the interested reader is referred to Chandar (2019).

In Windt et al. (2019a), a comparison between the overset grid implementation in *opera* and the native overset grid implementation in OpenFOAM v1812 is undertaken. As shown in Fig. 10, good agreement[5] is found between the two overset grid implementations. However, the implementation of the overset method in *opera* is observed to be more computationally efficient than the implementation in OpenFOAM v1812, delivering 1.42 times faster computation, in terms of run time, for the specific case study tested by Windt et al. (2019a).

## 5 Results and discussion

This section presents and discusses the results of the assessment of the overset grid method based on the five different test cases, introduced in Sect. 3.3.

[5] For the quantitative results, the interested reader is referred to Windt et al. (2019a).

### 5.1 Static equilibrium test

First, results for the static equilibrium test are presented in Fig. 11, where Fig. 11a–c shows the device displacement in the surge, heave, and pitch DoF, respectively. Fig. 11d–f shows the hydrodynamic forces and moments in the surge, heave, and pitch DoF, respectively. For all subfigures (and all subsequent plots in this Sect. 5, unless stated differently), the black solid line shows the results from *opera*, while the dashed red line refers to the results with mesh morphing.

A clear mismatch between *opera* and mesh morphing can be observed for all plotted quantities in Fig. 11. Overall, relatively small amplitudes of the device displacement are seen. The device displacement in the surge DoF shows an order of magnitude of $\mathcal{O}(10^{-4}\,\mathrm{m})$, an order of magnitude of $\mathcal{O}(10^{-3}\,\mathrm{m})$ in the heave DoF, and an order of magnitude of $\mathcal{O}(10^{-3}\,\mathrm{deg})$ in the pitch DoF. Similarly, the order of magnitude of the hydrodynamic forces are relatively small ($\mathcal{O}(10^{-2}\,\mathrm{N})$ in the surge DoF, $\mathcal{O}(10^{1}\,\mathrm{N})$ in the heave DoF, and $\mathcal{O}(10^{-2}\,\mathrm{N})$ in the pitch DoF). The plot of the heave displacement indicates an offset for the equilibrium position of the device simulated with *opera*. While the body oscillates around the equilibrium positions at 0m in the heave DoF for mesh morphing, the equilibrium position for *opera* is at approximately $-0.25 \times 10^{-3}\,\mathrm{m}$, which is reflected in the non-zero mean force ($\bar{Fz} \approx 1.25\,\mathrm{N}$). This small offset can be induced by a mismatch in the body volume, between the mesh morphing and opera setup, induced by slight differences in the mesh. Following $V = \frac{\bar{Fz}}{\rho g}$, the volume defect can be estimated as $V = 1.8 \times 10^{-4}$, which is 0.2% of the total device volume.

Comparing the different motion and force data recorded during the static equilibrium test to the WSI simulations (see Sects. 5.3 or 5.4), the observed WEC motion and forces on the WEC body are at least one or two orders of magnitude smaller. This indicates that, although qualitatively relatively large deviations can be observed between mesh morphing and *opera* for the static equilibrium test, these deviations have a negligible influence for WSI simulations.

Since the difference between the two data sets for mesh morphing and *opera*, for this test case, is relatively obvious from a qualitative comparison, no quantitative comparison is subsequently presented here.

Regarding the computational expense of the overset grid method, the relative runtime $t_\mathrm{r}$ is introduced, as

$$t_\mathrm{r} = \frac{t_\mathrm{r,o}}{t_\mathrm{r,MM}}, \tag{6}$$

where $t_\mathrm{r,MM}$ denotes the runtime for the mesh morphing method and $t_\mathrm{r,o}$ denotes the runtime of the overset grids method.

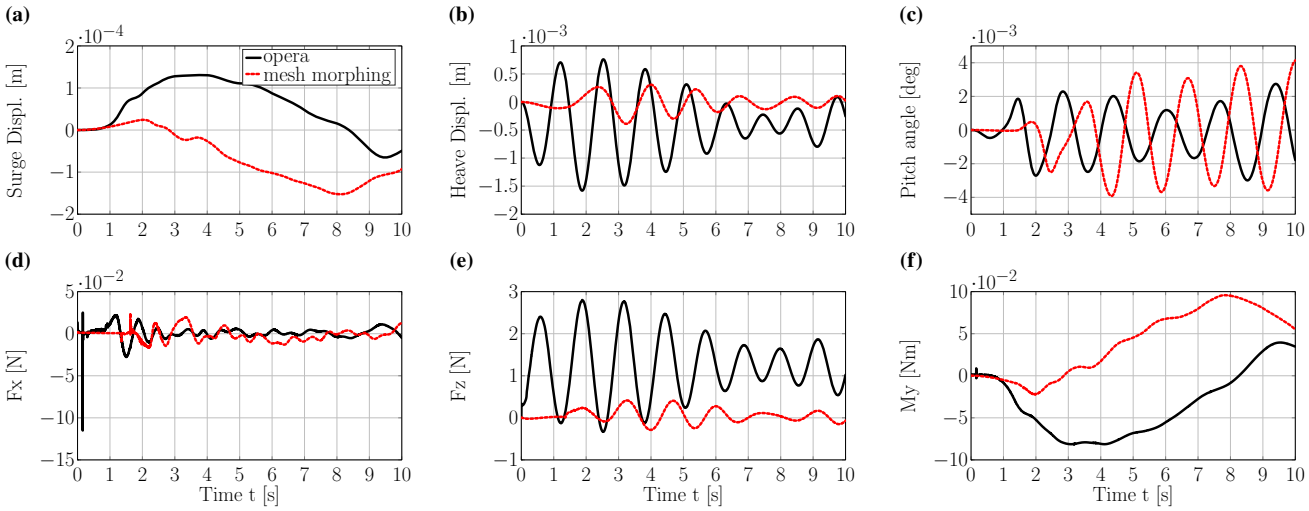


**Fig. 11** Heave, surge, and pitch displacements and forces during the free floating body test

For the static equilibrium test case, $t_r = 1.5$, indicating longer run times for the overset grid method, which is consistent with the findings by Windt et al. (2019a). For comparative purposes, Table 5 lists the relative runtime for the first four considered test cases.

## 5.2 Free decay test

Figure 12a, b shows the time traces of the displacement and hydrodynamic forces in the heave DoF, respectively, during the free decay test. A qualitative assessment of the results shows a closer match between the results from *opera* and mesh morphing, compared to the results of the static equilibrium test shown in Sect. 5.1. The results suggest that the larger order of magnitude of the device motion and hydrodynamic force blur the deviations observed for the static equilibrium test.

Generally, slightly larger motion and force amplitudes can be observed for the results from *opera*, compared to mesh morphing. Noteworthy are the spikes which can be observed in the force signal from *opera*; however, these spikes in the fluid force do not propagate to the motion of the device and seem to be smoothed out by the motion solver. At the time of writing, the authors were not able to identify the cause of the observed spikes and further analysis of similar test cases with different initial conditions should be performed in the future.

**Table 5** Runtime comparison between mesh morphing and *opera*

| Test case | $t_{r,o}/t_{r,MM}$ |
|---|---|
| Static equilibrium test | 1.5 |
| Free decay test | 2.0 |
| Wave excitation force test | 1.9 |
| Wave-induced motion—uncontrolled WEC | 2.0 |

$t_{r,MM}$ runtime mesh morphing, $t_{r,o}$ runtime overset grids

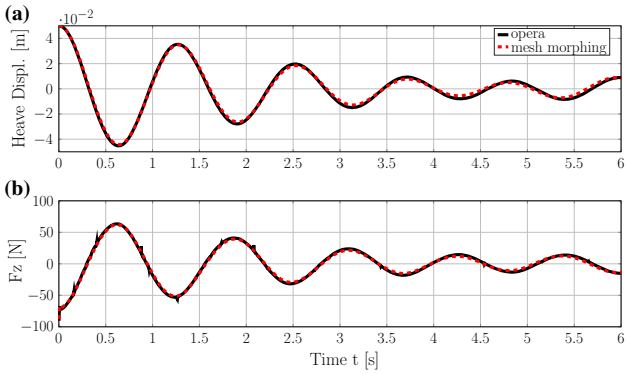


**Fig. 12** Heave displacement and forces during heave free decay test

For a quantitative assessment, the root-mean-squared deviation (nRMSD) is considered, following

$$\text{nRMSD} = \sqrt{\frac{\sum_{i=1}^{N}(y_{MM}(i) - y_o(i))^2}{N}} \cdot \frac{1}{n}, \tag{7}$$

where $N$ indicates the number of samples of the signal, $y_{MM}$ is the result from mesh morphing, and $y_o$ is the result from *opera*. $n$ is the normalisation factor.

For the case of the heave free decay test, the initial displacement, i.e., $n = 0.05\,\text{m}$, is considered for the normalisation of the RMSD of the heave displacement. For the heave force, $n$ is chosen to be the analytical hydrostatic force in the equilibrium position, i.e. $n = 634.14\,\text{N}$.

nRMSD values of 2.7% and 0.2% are calculated for the heave displacement and heave forces, respectively. These

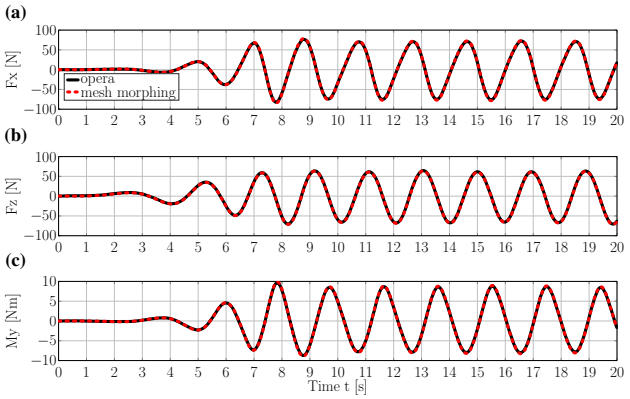


**Fig. 13** Forces on the fixed WEC, exposed to regular waves

deviations can be regarded as relatively small and are consistent with the findings by Windt et al. (2019a).

In terms of relative runtime, *opera* shows an increase in runtime, compared to mesh morphing, of a similar order of magnitude as for the static equilibrium test, i.e., $t_r = 2$.

### 5.3 Wave excitation forces on a fixed body

Figure 13a–c shows the wave excitation forces and moments in the surge, heave, and pitch DoF, respectively, from *opera* and mesh morphing. A qualitative inspection of the time traces from *opera* and mesh morphing show good agreement between the two dynamic mesh motion methods, similar to the heave free decay test. For the quantitative comparison, the nRMSD is considered, following Eq. (7), where the RMSD is normalised by the maximum force/moment magnitude. For the forces and moments in the surge, heave, and pitch DoFs, relatively small nRMSD values of 0.6% can be calculated, revealing also quantitatively good agreement between overset grids and mesh morphing. Since the device is fixed during the wave excitation force tests, and thus no mesh motion is allowed, any deviations are assumed to stem from interpolation in the overset grid method. From the relatively small nRMSD, it can, thus, be concluded that the interpolation errors are generally minimal.

Regarding the computational overhead, *opera* also shows an increased runtime, compared to mesh morphing, i.e., $t_r = 1.9$, for this test.

### 5.4 Wave-induced motion—uncontrolled WEC

Figure 14a–c shows the WEC displacement in the surge, heave, and pitch DoFs, respectively. Figure 14d–f shows the hydrodynamic forces and moments acting on the WEC device in the surge, heave, and pitch DoFs, respectively.

Similar to the free decay and wave excitation force test cases, a relatively good qualitative agreement between *opera* and mesh morphing can be observed. For the quantitative assessment, the nRMSD, following Eq. (7) is evaluated, where the RMSD is normalised by the maximum displacement or force/moment magnitude. nRMSD values of 3.9%, 0.4%, and 0.4% are calculated for the displacement in the surge, heave, and pitch DoFs, respectively. For the hydrodynamic forces in the surge and heave DoFs, and the moment in the pitch DoF, nRMSD values of 0.5%, 1.1%, and 4.5% are calculated, respectively.

Comparing the nRMSD values for the hydrodynamic forces for the case of the wave-induced motion test and the wave excitation force tests, larger deviations between mesh morphing and *opera* can be observed, specifically in the pitch DoF. The larger deviations could be attributed to either/both the required interpolation in the overset grid algorithm or/and the influence of the mesh deformation in the mesh morph-

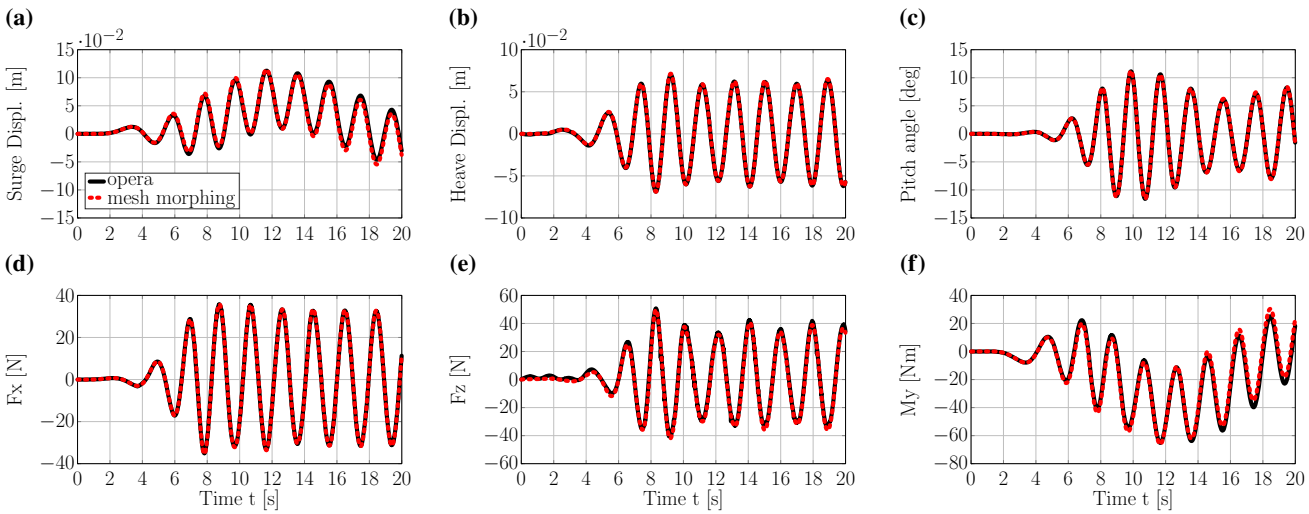


**Fig. 14** Heave, surge and pitch displacements and forces of the moving WEC, exposed to regular waves

ing, i.e., skewed cells with larger aspect ratios. For dynamic WSI simulations, compared to the static body in the wave excitation force test, the interpolation between the grids is more challenging, due to the varying interpolation partners, caused by the larger relative motion between the grids.

Regarding the relative runtime, opera shows an increase in runtime, consistent with the previously presented test cases, at $t_r = 2$.

## 5.5 Wave-induced motion—controlled WEC

This section assesses the performance of the overset grid method for a controlled WEC in operational conditions, by considering an irregular sea state, comparing against the mesh morphing method, and contrasting motion of and controlled and uncontrolled WEC.

### 5.5.1 Mesh morphing

Figure 15a–c shows the surge, heave, and pitch displacement of the uncontrolled (black solid) and controlled (dash red) WEC device, respectively. For the case of the uncontrolled WEC, it can be observed that the WEC surges in the wave propagation direction, and oscillates back due to the mooring forces, with a maximum displacement of 0.25 m (from its equilibrium position). In heave, a maximum displacement amplitude of approx. 0.1 m is measured at $t = 88$s, while a maximum pitch angle of approx. 20° can be measured at $t = 41$ s. For the case of the controlled device, a clear increase in device motion, most significantly in surge motion, can be observed. Results for the controlled WEC, modelled with mesh morphing, are only available up to 50.2 s, at which the simulation crashes.

Figure 15 shows screenshots of the CFD-based numerical wave tank, for an uncontrolled and controlled WEC cases, taken at four different time instances, representing: equal motion for the controlled and uncontrolled case ($t = 23$ s), larger heave displacement in the controlled case, with similar surge and pitch motion ($t = 35$ s), larger pitch and surge displacement in the controlled case, with similar heave motion ($t = 46$ s), and the last time instance for the controlled device before the simulation crashes ($t = 50.2$ s). At $t = 50.2$ s, the mesh, down-wave of the controlled WEC, is highly skewed, causing numerical instabilities due to the high cell non-orthogonality. The *checkMesh* toolbox, implemented in OpenFOAM, indicates 88 additional, severely non-orthogonal faces and 30 incorrectly oriented faces at $t = 50.2$ s. Overall, the results highlight the importance of using advanced mesh motion methods for WEC control studies.

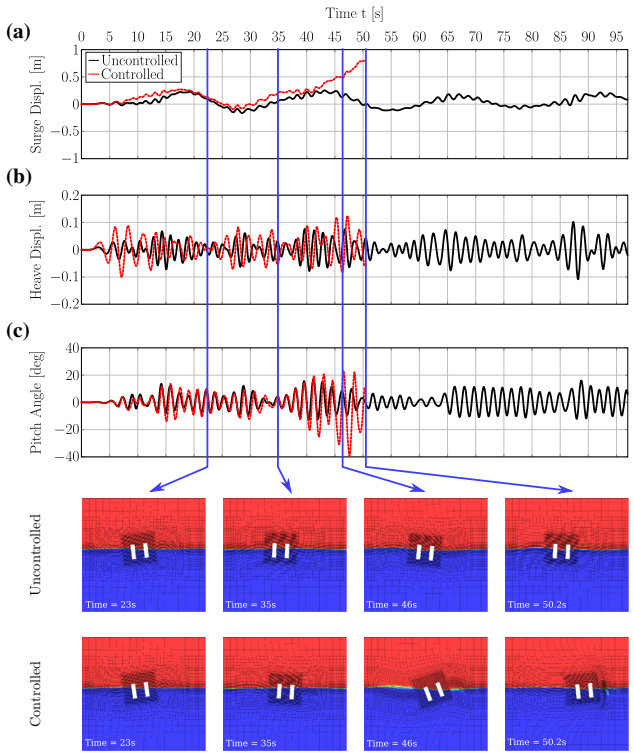


**Fig. 15** Heave, surge and pitch displacements of the uncontrolled and controlled WEC device, modelled with mesh morphing, exposed to irregular waves. Additionally, the mesh deformation in the CFD-based numerical wave tank for the mesh morphing method is shown. After 50.2 s, the simulation of the controlled WEC aborts, due to poor mesh quality

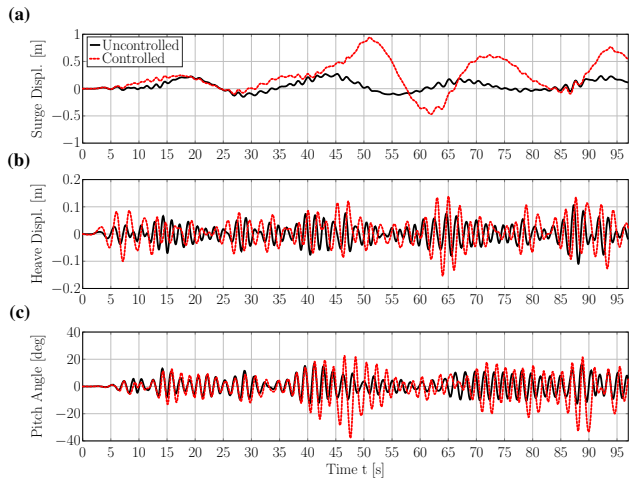


**Fig. 16** Heave, surge and pitch displacements of the uncontrolled and controlled WEC device, modelled with *opera*, exposed to irregular waves

### 5.5.2 Opera

Figure 16a–c shows the surge, heave, and pitch displacement of the uncontrolled (black solid) and controlled (dash

red) WEC device, respectively. Again, the enhanced device motion under controlled conditions is highlighted. The WEC surges in the wave propagation direction with a maximum displacement of 1 m (from its equilibrium position) (at $t \approx 50$ s). In heave, the maximum amplitude is 0.12 m (at $t = 64$ s), while a maximum pitch angle of $-40°$ is measured at $t = 48$ s.

For a better comparison between the results from mesh morphing and overset grids, Fig. 17a–c shows the surge, heave, and pitch displacement of the uncontrolled WEC, modelled with the mesh morphing (red dashed) and *opera* (solid black). For the case of the uncontrolled WEC, the device follows the same trajectory, when modelling with *opera* or mesh morphing, which is consistent with the findings in Sects. 5.1–5.4. For the case of the controlled WEC (see Fig. 17d–f), the trajectories for the surge, heave and pitch displacement, too, show similar results when modelled with *opera* or mesh morphing; however, modelling the controlled

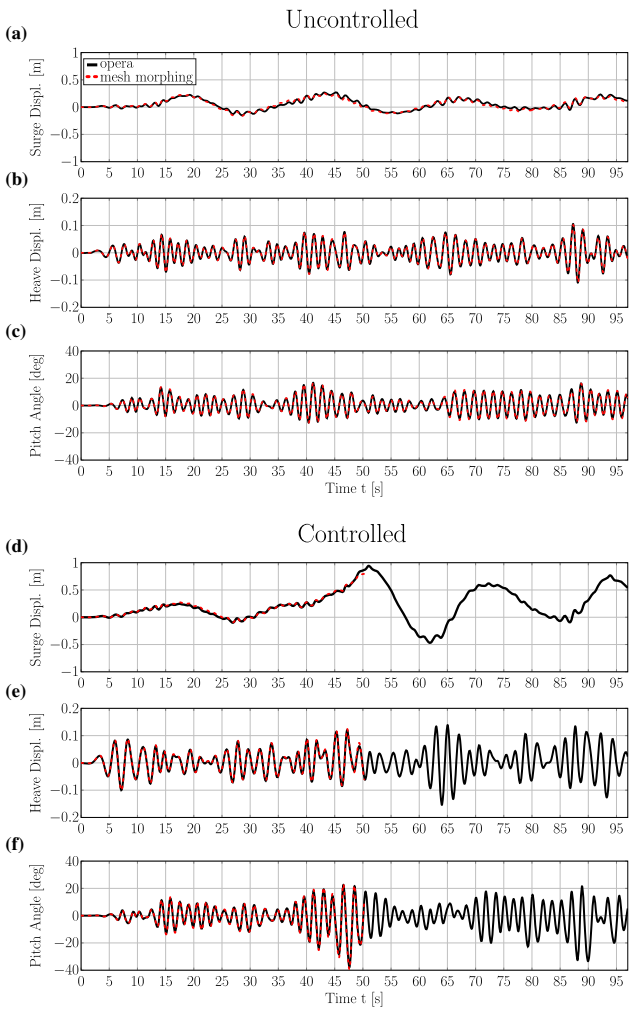


**Fig. 17** Heave, surge and pitch displacements of the uncontrolled and controlled WEC device, modelled with *opera* and mesh morphing, exposed to irregular waves

WEC with *opera* allows simulation of the complete sea state, avoiding any limitations induced by poor mesh quality.

## 6 Conclusions

The performance of the overset grid method is evaluated, by comparing the hydrodynamic forces and body motions of a moored point absorber WEC, simulated using the overset grid against simulations using the mesh morphing method, for several test cases with increasing levels of complexity. From the results, it can be concluded that the accuracy of the overset grid method, implemented in OpenFOAM through the *opera* toolbox, is equivalent to the mesh morphing method, but is better able to handle the large amplitude WEC motions during control studies. However, the drawback of the overset grid method is an approximate twofold increase to the run time. To avoid unnecessary computational cost, CFD engineers are, thus, advised to assess beforehand, if the mesh morphing method exceeds the limits of numerical stability.

**Acknowledgements** This paper is based upon work supported by Science Foundation Ireland under Grant no. 13/IA/1886. Josh Davidson is supported by the Higher Education Excellence Program of the Ministry of Human Capacities in the frame of Water science & Disaster Prevention research area of Budapest University of Technology and Economics (BME FIKP-VÍZ).

## References

Atan R, Goggins J, Nash S (2016) A detailed assessment of the wave energy resource at the atlantic marine energy test site. Energies 9(11):967

Balitsky P, Bacelli G, Ringwood JV (2014) Control-influenced layout optimization of arrays of wave energy converters. In: ASME, (2014) 33rd international conference on ocean. Offshore and Arctic Engineering, San Francisco, CA, USA

Berberović E, van Hinsberg NP, Jakirlić S, Roisman IV, Tropea C (2009) Drop impact onto a liquid layer of finite thickness: dynamics of the cavity evolution. Phys Rev E 79:036306-1–036306-15

Bharath A, Nader J-R, Penesis I, Macfarlane G (2018) Nonlinear hydrodynamic effects on a generic spherical wave energy converter. Renew Energy 118:56–70

Chandar DD (2019) On overset interpolation strategies and conservation on unstructured grids in openfoam. Comput Phys Commun 239:72–83

Chen H, Qian L, Ma Z, Bai W, Li Y, Causon D, Mingham C (2019a) Application of an overset mesh based numerical wave tank for modelling realistic free-surface hydrodynamic problems. Ocean Eng 176:97–117

Chen H, Qian L, Ma Z, Bai W, Lin Z (2019b) CCP-WSI blind test series 3: OpenFOAM simulation of focused wave interaction with a simplified wave energy converter. In: Proceedings of the twenty-ninth (2019) international ocean and polar engineering conference. Honolulu, Hawaii, USA

Coe RG, Rosenberg BJ, Quon EW, Chartrand CC, Yu Y-H, van Rij J, Mundon TR (2019) CFD design-load analysis of a two-body wave energy converter. J Ocean Eng Mar Energy 5:1–19

Coiro DP, Troise G, Calise G, Bizzarrini N (2016) Wave energy conversion through a point pivoted absorber: numerical and experimental tests on a scaled model. Renew Energy 87:317–325

Davidson J, Karimov M, Szelechman A, Windt C, Ringwood J (2019) Dynamic mesh motion in openfoam for wave energy converter simulation. In: 14th OpenFOAM Workshop

Davidson J, Windt C, Giorgi G, Genest R, Ringwood J (2018) Chapter: evaluation of energy maximising control systems for wave energy converters using OpenFOAM. OpenFOAM—selected papers from the 11th workshop

Elhanafi A, Macfarlane G, Fleming A, Leong Z (2017a) Experimental and numerical investigations on the hydrodynamic performance of a floating-moored oscillating water column wave energy converter. Appl Energy 205:369–390

Elhanafi A, Macfarlane G, Fleming A, Leong Z (2017b) Experimental and numerical investigations on the intact and damage survivability of a floating-moored oscillating water column device. Appl Ocean Res 68:276–292

ESI (2017) OpenFOAM v1712 release notes: new and improved numerics. https://www.openfoam.com/releases/openfoam-v1712/numerics.php#numerics-overset

ESI (2018) OpenFOAM v1812 release notes: new and improved numerics. https://www.openfoam.com/releases/openfoam-v1812/numerics.php#numerics-overset

Faedo N, Scarciotti G, Astolfi A, Ringwood JV (2018) Energy-maximising control of wave energy converters using a moment-domain representation. Control Eng Pract 81:85–96

Falcao A (2010) Wave energy utilization: a review of the technologies. Renew Sustain Energy Rev 14:899–918

Ferziger JH, Peric M (2001) Computational methods for fluid dynamics. Springer, Berlin

Folley M (ed) (2016) Numerical modelling of wave energy converters. Academic Press, New York

Garcia-Rosa PB, Bacelli G, Ringwood JV (2015) Control-informed optimal array layout for wave farms. IEEE Trans Sustain Energy 6(2):575–582

Giorgi G, Penalba M, Ringwood J (2016) Nonlinear hydrodynamic models for heaving buoy wave energy converters. In: Proceedings of the 3rd Asian wave and tidal energy conference, Marina Bay Sands, Singapore

Giorgi G, Ringwood JV (2017) Computationally efficient nonlinear Froude–Krylov force calculations for heaving axisymmetric wave energy point absorbers. J Ocean Eng Mar Energy 3(1):21–33

Goldhirsch I, Sulem P-L, Orszag SA (1987) Stability and lyapunov stability of dynamical systems: a differential approach and a numerical method. Phys D 27(3):311–337

Goodwin GC, Graebe SF, Salgado ME (2001) Control system design, vol 240. Prentice Hall, New Jersey

Higuera P, Lara JL, Losada IJ (2013) Simulating coastal engineering processes with OpenFOAM®. Coast Eng 71:119–134

Hirt CW, Nichols BD (1981) Volume of fluid (VOF) method for the dynamics of free boundaries. J Comput Phys 39:201–225

Jung MS, Kwon OJ (2009) A parallel unstructured overset mesh technique for unsteady flow simulations. Springer, Berlin

Kim JW, Jang H, Baquet A, O'Sullivan J, Lee S, Kim B, Jasak H (2016) Technical and economic readiness review of CFD-based numerical wave basin for offshore floater design. In: Proceedings of the (2016) offshore technology conference. Houston, TX, USA

Mankins JC (1995) Technology readiness levels. Technical report, Office of Space Access and Technology, NASA

Menter FR (1992) Improved two-equation kâω turbulence models for aerodynamic flows. Technical report, NASA Technical Memorandum TM-103975

Mérigaud A, Ringwood JV (2017) Free-surface time-series generation for wave energy applications. IEEE J Ocean Eng 43(1):19–35

Morison J, Johnson J, Schaaf S (1950) The force exerted by surface waves on piles. J Petrol Technol 2:149–154

OpenFOAM Foundation (2014) OpenFOAM 2.3.0 release notes: mesh motion. https://openfoam.org/release/2-3-0/mesh-motion/

Penalba M, Giorgi G, Ringwood JV (2017a) Mathematical modelling of wave energy converters: a review of nonlinear approaches. Renew Sustain Energy Rev 78:1188–1207

Penalba M, Touzón I, Lopez-Mendia J, Nava V (2017b) A numerical study on the hydrodynamic impact of device slenderness and array size in wave energy farms in realistic wave climates. Ocean Eng 142:224–232

Ransley E, Yan S, Brown S, Musiedlak P-H, Windt C, Schmitt P, Davidson J, Ringwood J, Wang J, Wang J, Ma Q, Xie Z, Zhang N, Zheng X, Giorgi G, Chen H, Lin Z, Qian L, Ma Z, Bai W, Chen Q, Zang J, Ding H, Cheng L, Zheng J, Gu H, Gong X, Liu Z, Zhuang Y, Wan D, Bingham H, Greaves D (2019) A blind comparative study of focused wave interactions with floating structures (CCP-WSI Blind Test Series 3). Int J Offshore Polar Eng

Ringwood JV, Bacelli G, Fusco F (2014) Energy-maximizing control of wave-energy converters: the development of control system technology to optimize their operation. IEEE Control Syst 34:30–55

Schmitt P, Elsässer B (2017) The application of Froude scaling to model tests of oscillating wave surge converters. Ocean Eng

Sharkey F, Bannon E, Conlon M, Gaughan K (2011) Dynamic electrical ratings and the economics of capacity factor for wave energy converter arrays. In: Proceedings of the 9th European wave and tidal energy conference, Southampton, UK

Shen Z, Wan D, Carrica P (2015) Dynamic overset grids in openfoam with application to KCS self-propulsion and maneuvering. Ocean Eng

Stansby P, Gu H, Moreno EC, Stallard T (2015) Drag minimisation for high capture width with three float wave energy converter M4. In: Proceedings of the 11th European wave and tidal energy conference, Nantes, France

STAR-CCM+ (2019) STAR-CCM+ webiste. https://mdx.plm.automation.siemens.com/star-ccm-plus

Thompson J (1999) Handbook of grid generation. CRC Press, Boca Raton

van Rij J, Yu Y-H, Guo Y, Coe RG (2019) A wave energy converter design load case study. J Mar Sci Eng 7:1–22

Windt C, Davidson J, Akram B, Ringwood JV (2018a) Performance assessment of the overset grid method for numerical wave tank experiments in the openfoam environment. In: ASME 2018 37th international conference on ocean, offshore and arctic engineering, V010T09A006–1–V010T09A006–10. American Society of Mechanical Engineers

Windt C, Davidson J, Ringwood JV (2018b) High-fidelity numerical modelling of ocean wave energy systems: a review of computational fluid dynamics-based numerical wave tanks. Renew Sustain Energy Rev 93:610–630

Windt C, Davidson J, Chandar D, Ringwood J (2019a) On the importance of advanced mesh motion methods for WEC experiments in CFD-based numerical wave tanks. In: Proceedings of the VIII international conference on computational methods in marine engineering, Gothenburg

Windt C, Davidson J, Chandar D, Ringwood J (2019b) On the importance of advanced mesh motion methods for WEC experiments in CFD-based numerical wave tanks. In: Presentation at the VIII international conference on computational methods in marine engineering, Gothenburg. https://www.researchgate.net/publication/334942092_On_the_importance_of_advanced_mesh_motion_methods_for_WEC_experiments_in_CFD-based_numerical_wave_tanks

Windt C, Davidson J, Ransley E, Greaves D, Jakobsen M, Kramer M, Ringwood J (2019c) Validation of a CFD-based numerical wave tank model for the power production assessment of the Wavestar ocean wave energy converter. Renew Energy 146:2499–2516

Windt C, Davidson J, Schmitt P, Ringwood J (2019d) CCP-WSI blind test series 3: CFD-based numerical wave tank experiments employing an impulse source wave maker. Int J Offshore Polar Engi

Windt C, Davidson J, Schmitt P, Ringwood J (2019e) Contribution to the CCP-WSI blind test series 2: CFD-based numerical wave tank experiments employing an impulse source wave maker. In: Proceedings of the 13th European wave and tidal energy conference, Naples, Italy

Windt C, Davidson J, Schmitt P, Ringwood J (2019f) Contribution to the CCP-WSI blind test series 3: analysis of scaling effects of moored point-absorber wave energy converters in a CFD-based numerical wave tank. In: Proceedings of the international society of offshore and polar engineers (ISOPE) conference (2019) Honolulu. HI, USA

Windt C, Davidson J, Schmitt P, Ringwood JV (2019g) On the assessment of numerical wave makers for CFD simulations. J Mar Sci Eng 7:2

Windt C, Faedo N, Ringwood JV (2019h) Assessment of the evaluation framework for energy maximising control systems for the wavestar wave energy converter. In: Proceedings of the 2019 American control conference (ACC), Philadelphia, USA, pp 4791–4796

# Terms and Conditions

Springer Nature journal content, brought to you courtesy of Springer Nature Customer Service Center GmbH (“Springer Nature”).
Springer Nature supports a reasonable amount of sharing of research papers by authors, subscribers and authorised users (“Users”), for small-scale personal, non-commercial use provided that all copyright, trade and service marks and other proprietary notices are maintained. By accessing, sharing, receiving or otherwise using the Springer Nature journal content you agree to these terms of use (“Terms”). For these purposes, Springer Nature considers academic use (by researchers and students) to be non-commercial.
These Terms are supplementary and will apply in addition to any applicable website terms and conditions, a relevant site licence or a personal subscription. These Terms will prevail over any conflict or ambiguity with regards to the relevant terms, a site licence or a personal subscription (to the extent of the conflict or ambiguity only). For Creative Commons-licensed articles, the terms of the Creative Commons license used will apply.
We collect and use personal data to provide access to the Springer Nature journal content. We may also use these personal data internally within ResearchGate and Springer Nature and as agreed share it, in an anonymised way, for purposes of tracking, analysis and reporting. We will not otherwise disclose your personal data outside the ResearchGate or the Springer Nature group of companies unless we have your permission as detailed in the Privacy Policy.
While Users may use the Springer Nature journal content for small scale, personal non-commercial use, it is important to note that Users may not:

1. use such content for the purpose of providing other users with access on a regular or large scale basis or as a means to circumvent access control;
2. use such content where to do so would be considered a criminal or statutory offence in any jurisdiction, or gives rise to civil liability, or is otherwise unlawful;
3. falsely or misleadingly imply or suggest endorsement, approval , sponsorship, or association unless explicitly agreed to by Springer Nature in writing;
4. use bots or other automated methods to access the content or redirect messages
5. override any security feature or exclusionary protocol; or
6. share the content in order to create substitute for Springer Nature products or services or a systematic database of Springer Nature journal content.

In line with the restriction against commercial use, Springer Nature does not permit the creation of a product or service that creates revenue, royalties, rent or income from our content or its inclusion as part of a paid for service or for other commercial gain. Springer Nature journal content cannot be used for inter-library loans and librarians may not upload Springer Nature journal content on a large scale into their, or any other, institutional repository.
These terms of use are reviewed regularly and may be amended at any time. Springer Nature is not obligated to publish any information or content on this website and may remove it or features or functionality at our sole discretion, at any time with or without notice. Springer Nature may revoke this licence to you at any time and remove access to any copies of the Springer Nature journal content which have been saved.
To the fullest extent permitted by law, Springer Nature makes no warranties, representations or guarantees to Users, either express or implied with respect to the Springer nature journal content and all parties disclaim and waive any implied warranties or warranties imposed by law, including merchantability or fitness for any particular purpose.
Please note that these rights do not automatically extend to content, data or other material published by Springer Nature that may be licensed from third parties.
If you would like to use or distribute our Springer Nature journal content to a wider audience or on a regular basis or in any other manner not expressly permitted by these Terms, please contact Springer Nature at

onlineservice@springernature.com